ACS APPLIED MATERIALS & INTERFACES

www.acsami.org

Research Article

An Electrical Stimulation-Driven Strategy for Peroxide-like Enzyme Reactivation toward Sustainable Wastewater Sterilization

Jingyang Fang, Guopeng Xu, Paul K. Chu, Jianzhong Du,* and Guomin Wang*

Cite This: *ACS Appl. Mater. Interfaces* 2025, 17, 56762−56772

Read Online

ACCESS | Metrics & More | Article Recommendations | Supporting Information

ABSTRACT: Metal-based enzyme mimics face irreversible deactivation due to the oxidation of active metal centers, limiting their sustainability in wastewater treatment. To meet this important challenge, we introduce an electrical stimulation strategy by designing Fe-doped titanium dioxide nanolines (Fe-TNLs) that mimic peroxidase (POD) activity and regenerate catalytic function, enabling enzyme reuse. The Fe-TNLs exhibit robust POD-like activity by catalyzing the decomposition of H_2O_2 into hydroxyl radicals ($^{\bullet}OH$), achieving over 99.9% inactivation against*Escherichia coli* and *Staphylococcus aureus* during the initial cycle. Unlike conventional Fe-based POD mimics, which are rapidly deactivated due to the oxidation of Fe(II) to Fe(III), this system achieves a reversible Fe(III)/Fe(II) redox cycle through electrical charging, restoring over 80% of the initial catalytic efficiency. Moreover, the reactivated Fe-TNLs maintain effective performance in simulated wastewater and retain approximately 60% of their initial efficacy after reactivation, outperforming single-use systems. By emphasizing sustainable reusability over single-use designs, this work offers a compelling approach for advancing environmentally friendly wastewater remediation technologies.

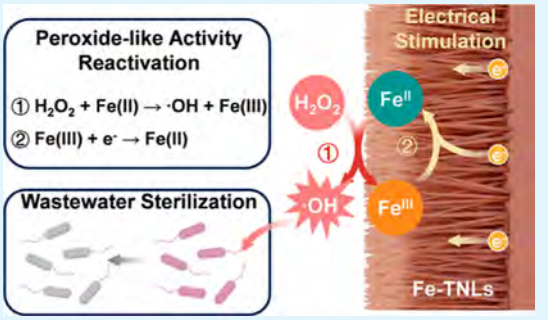

KEYWORDS: *wastewater treatment, TiO_2, enzyme, peroxidase, antibacterial*

INTRODUCTION

The coexistence of pathogenic microorganisms and organic pollutants in water pollution poses a severe threat to public health and ecosystems.[1−3] Conventional water treatment technologies, such as chlorination, effectively inactivate bacteria but carry risks of generating toxic byproducts.[4] Advanced oxidation processes based on reactive oxygen species (ROS) have emerged as promising alternatives due to their broad-spectrum antimicrobial and pollutant degradation capabilities.[5−7] Among these, transition metal-based nanomaterials, such as iron, for example, have garnered attention for their enzyme-like catalytic activity, which enables sustainable ROS generation. For instance, the Fenton process leverages Fe(II)-containing peroxidase (POD)-mimetic materials to decompose hydrogen peroxide (H_2O_2) under mild conditions, producing highly reactive hydroxyl radicals ($^{\bullet}OH$) that inactivate microbes and oxidize organic pollutants.[8] However, the irreversible oxidation from Fe(II) to Fe(III) during reactions leads to active site deactivation.[9,10]

The enzymic efficiency can be elevated by enhancing the durability and reusability, which conventionally rely on chemical modifications and physical stabilization methods.[11,12] Restoring the tertiary structure of enzymes or improving their microenvironment through external interventions can prolong the enzymatic activity.[13,14] However, they often suffer from unclear targeting, low efficiency, and limited reuse cycles.[15,16] Achieving reusability is more valuable than merely enhancing the durability. Emerging strategies, such as encapsulating enzymes within dynamic-responsive nanostructures, enable reversible regulation of enzyme activity.[17,18] For transition metal-based POD-like enzymes, current research has explored the addition of exogenous reducing agents to restore activity[19] or the direct replenishment of reduced metal ions.[20,21] These methods are often hampered by the high cost and complexity of the process, which prevent them from being used on a large scale. As electron transfer is a key mechanism in the catalytic reactions of certain enzymes, electrical intervention at the interface can work efficiently to adjust the enzymic activity. On the one hand, electrochemistry is a simple and rapid method that can enhance the activity of some transition metal-based enzymes.[22,23] Meanwhile, electrical stimulating methods have been demonstrated to induce a reduction reaction at the surface of the material, thereby facilitating valence state transitions in transition metal materials.[24,25] Hence, electrical stimulation holds great promise for restoring catalytic activity without the need for chemical additives. However, the

Received: July 2, 2025
Revised: August 22, 2025
Accepted: September 24, 2025
Published: September 30, 2025

feasibility of this hypothesis and its underlying mechanisms have rarely been explored.

Here, we present a rechargeable Fe(III)/Fe(II) redox-cycling enzymatic platform and introduce an electrical stimulation strategy to restore the enzymatic activity. A titanium dioxide nanoline (TNL) scaffold with a high surface area is first fabricated to provide robust mechanical and chemical stabilities while effectively supporting enzyme immobilization.[26,27] Subsequently, highly dispersed Fe-containing POD-like nanoparticles are hydrothermally anchored onto the TNL surface. This design synergistically harnesses the intrinsic POD-like enzymatic properties of Fe and the activity-regenerating capability of electrical stimulation to enable a sustained catalytic performance. In this system, Fe nanoparticles function as active centers that mimic POD, catalyzing the decomposition of H_2O_2 into ROS for the disinfection of bacteria in wastewater. Crucially, electrical stimulation recharging restores the catalytic cycle by reducing Fe(III) back to Fe(II), thus overcoming the irreversible deactivation typically observed in conventional enzyme-mimetic systems. By addressing this critical limitation, the Fe-TNL composite offers a scalable and cost-effective solution for continuous microbial inactivation. These findings underscore the promise of rechargeable catalytic systems for tackling complex water contamination challenges and provide a foundation for the development of environmentally adaptive remediation technologies.

METHODS AND MATERIALS

Materials. Titanium sheets were purchased from Shengyuan Metal Materials (China). $FeCl_3{\cdot}6H_2O$, dimethyl sulfoxide (DMSO) and 3,3′,5,5′-tetramethylbenzidine (TMB) were purchased from Sigma-Aldrich (Germany). LB broth medium and nutrient agar were purchased from Hope Bio-Technology Co., Ltd. (China). All other chemical agents were purchased from Adamas Beta (China) without further purification. Ultrapure water (Millipore Milli-Q grade, 18.2 MΩ) was used to prepare the buffers and solutions.

Preparation of TNLs. Titanium sheets with dimensions of 10 × 10 × 1 mm^3 were selected as the substrates. TNLs were synthesized by a wet oxidation process. Twenty-five mL of the melamine solution (0.0040 g mL^{-1}), 25 mL of hydrogen peroxide (30 wt %), and 1.0 mL of nitric acid (65 wt %) were mixed ultrasonically. Afterward, clean titanium sheets were placed in the solution. The synthesis was carried out in a blast oven at 80 °C for 12 h, and TNLs were formed on the substrate. After the reaction, the samples were washed with deionized water and dried at room temperature. TNLs were then annealed in a tube furnace at 850 °C for 1.5 h in an air atmosphere for stabilization.

Construction of Fe-TNLs. $FeCl_3{\cdot}6H_2O$ (0.3 M) was dissolved in ultrapure water. The resulting solution and the TNL sheets were transferred to a Teflon-lined stainless-steel autoclave heated at 200 °C for 2 h. After the mixture was naturally cooled to room temperature, the product color changed from gray to coral. Finally, Fe-TNLs were dried in an air-blowing thermostatic oven.

Characterization of Fe-TNLs. Scanning electron microscopy (SEM) images were measured on a microscope (GeminiSEM 300, ZEISS, Germany). X-ray photoelectron spectroscopy (XPS) and valence band spectra were recorded with a spectrometer (Thermo Fisher Scientific, K-Alpha, USA). X-ray diffraction (XRD) patterns were recorded with an X-ray diffractometer (Rigaku SmartLab SE, Japan). Energy-dispersive spectroscopy (EDS) images were measured on a Spectrometer (Xplore 30, OXFORD, UK).

POD-like Activity Measurement. The POD-like activity of Fe-TNLs was evaluated using TMB (dissolved in DMSO) as the substrate in the presence of H_2O_2. Typically, TMB (0.25 mM) and H_2O_2 (0.25 mM) were added to 0.5 mL of HAc-NaAc buffer (0.2 M; pH 4.5). Then, the mixture was dropped on the surface of Fe-TNLs. Finally, the UV−vis absorbance spectra of oxidized TMB (oxTMB) were recorded at a certain reaction time to evaluate the POD-like activity, which were obtained via characterization on a multimode microplate reader (Spark, Tecan, Switzerland) under room temperature.

Enzymatic Activity Evaluation and Catalytic Kinetic Assay. The UV−vis absorbance spectra of oxTMB were recorded to evaluate the POD-like activity of Fe-TNLs. All of the catalytic reactions were conducted at room temperature. The steady-state kinetic assay of Fe-TNLs on H_2O_2/TMB was conducted by adding Fe-TNLs into HAc−NaAc buffer solution (pH 4.5) containing fixed TMB (2.0 mM)/H_2O_2 (2.0 mM) and various concentrations of H_2O_2 (0.05, 0.1, 0.2, 0.5, 1.0, 2.0, 3.0, and 5.0 mM)/TMB (0.05, 0.1, 0.2, 0.3, 0.5, 1.0, 2.0, and 3.0 mM). The Michaelis constant (K_m) was defined as the substrate concentration at half of the maximum reaction rate that reflects the substrate affinity of the nanozymes. The maximal reaction velocity (V_{max}) was the maximum reaction rate at a saturated substrate concentration. K_m and V_{max} were calculated by fitting the initial reaction velocity values (V) and substrate concentrations to the Michaelis−Menten equation.

The Reactivation of POD-like Activity of Fe-TNLs. The reactivation of POD-like activity was achieved through the following electrical stimulation procedure: the used Fe-TNLs served as the working electrode in a three-electrode system connected to an electrochemical workstation (CHI660e, CH Instruments Co., Ltd., China). A platinum electrode and a saturated calomel electrode (SCE) were employed as the counter and reference electrodes, respectively. The electrolyte consisted of a HAc−NaAc buffer solution (pH 4.5). Cyclic voltammetry (CV) was performed with a scan potential range of −1.5 to 1.5 V (vs SCE), a scan rate of 0.1 V/s, and a duration of 15 min. After being charged, the Fe-TNLs were extracted, rinsed, and air-dried for subsequent usage.

Iron Loss Test. The inductively coupled plasma optical emission spectrometer (ICP−OES) (5110, Agilent, USA) was introduced to determine the content of iron released from Fe-TNLs after incubation in water for different times. The centrifuge tubes containing Fe-TNLs were filled with 50 mL of ultrapure water; after incubation for 15, 30, and 45 min, the solution was collected in tubes, respectively. Then, the samples were introduced to be tested in the ICP−OES instrument for their characteristic spectral intensity.

Radical Species Measurements. The electron spin resonance (ESR) spin trapping technique was introduced to detect radical species with a spin trap, 5,5-dimethyl-1-pyrroline *N*-oxide (DMPO). Fe-TNLs were prepared, and H_2O_2 was prepared in phosphate buffer (0.2 M, pH 4.5), including DMPO (0.88 M). The ESR measurements were taken under the following conditions: microwave power, 6.38 mW; modulation amplitude, 1.00 G; modulation frequency, 100.00 kHz; conversion time, 41.00 ms.

In Vitro Antibacterial Activity. The antibacterial activity of Fe-TNLs against Gram-negative *Escherichia coli* (ATCC entry 8739) and Gram-positive *Staphylococcus aureus* (ATCC entry 6538P) was evaluated by the standard plate counting method. Experiments were divided into four groups as follows:

(I) control (no treatment);
(II) H_2O_2;
(III) Fe-TNLs;
(IV) Fe-TNLs + H_2O_2.

The final concentrations of bacteria and H_2O_2 were 10^7 colony-forming units (cfus) mL^{-1}, and 100 μM, respectively. Then, the mixtures of each group were dropped on the surface of the Fe-TNLs individually. After incubation for 60 min, the mixture in each group was diluted 10^5-fold. Afterward, 100 μL of the dilution was placed on a solid medium and cultured at 37 °C for 18 h. Finally, the number of cfus was counted to calculate the antibacterial rate using the following equation

$$\text{antibacterial rate} = \left[1 - \frac{\text{cfu(each group)}}{\text{cfu(I)}}\right] \times 100\%$$

https://doi.org/10.1021/acsami.5c12970
ACS Appl. Mater. Interfaces 2025, 17, 56762−56772

Scheme 1. Schematic Illustration of the Preparation of Fe-Doped Titanium Dioxide Nanolines for Sustainable Wastewater Sterilization with Electrically Stimulated Regeneration of POD-like Activity[a]

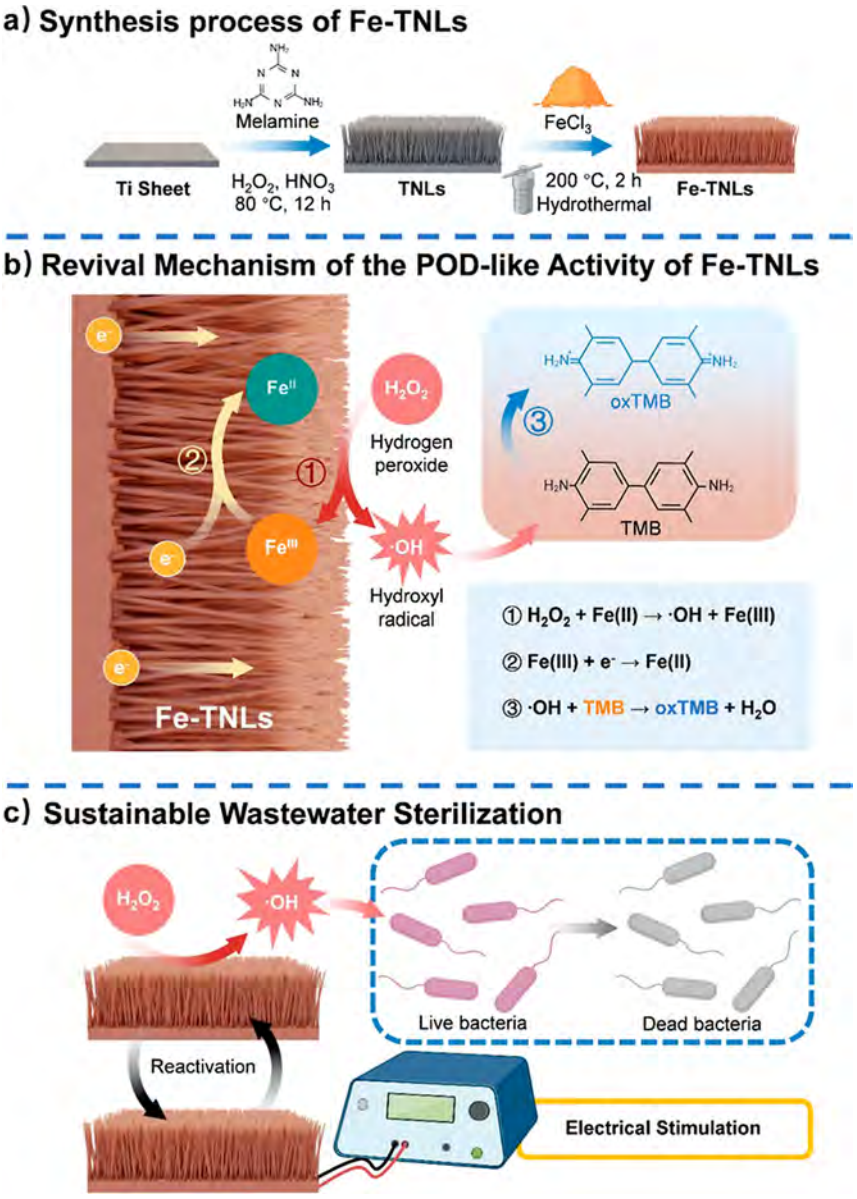

[a](a) Titanium dioxide nanolines (TNLs) are synthesized using a chemical dissolution-nucleation technique, followed by the preparation of Fe-doped TNLs (Fe-TNLs) via a hydrothermal method. (b) Fe(II) within Fe-TNLs reacts with hydrogen peroxide (H_2O_2), generating Fe(III) and hydroxyl radicals ($^{\bullet}OH$), exhibiting a POD-like activity. Subsequently, electrical stimulation reduces Fe(III) back to Fe(II), restoring the POD-like activity. The generated $^{\bullet}OH$ radicals oxidize 3,3′,5,5′-tetramethylbenzidine (TMB) to form a blue oxidation product (oxTMB), providing a chromogenic method to confirm the POD-like activity of Fe-TNLs. (c) Regeneration of the POD-like activity in Fe-TNLs via electrical stimulation allows for their repeated use in wastewater sterilization.

where cfu(I) is the cfu value of group I and cfu (each group) is the cfu value of groups II–IV.

Antimicrobial Activity in Synthetic Wastewater. The antibacterial activity of Fe-TNLs against Gram-negative *E. coli* in synthetic wastewater was evaluated by the standard plate counting method. In this experiment, synthetic wastewater with *E. coli*, which has been described in the main text, was used in place of the bacterial solution for the antimicrobial experiments. The groupings were the same as those in the above text. The number of cfu was counted to calculate bacterial viability using the equation above, as well.

Observation of Bacterial Morphology. Bacteria were first treated following procedures in the plate counting assay and then fixed with paraformaldehyde (4 wt %) for 2 h. After that, fixed samples were serially dehydrated at different concentrations of ethanol (30, 50, 70, 90, and 100%), each for 10 min, with the remaining liquid removed during each session. The dehydrated samples were then dried in air. Finally, all of the samples were coated with gold for SEM observation.

Live/Dead Fluorescence Staining to Evaluate the Viability of Bacteria. A fluorescence microscope was utilized to visualize live/dead bacteria stained with the LIVE/DEAD Bacterial Staining Kit and DMAO & PI (C2030s, Beyotime Biotechnology Co., Ltd., China). Bacteria were treated as in the plate counting assay, and then the mixture was incubated with DMAO/PI for 20 min in the dark. Finally, stained bacteria were observed under an inverted fluorescence microscope.

Intracellular ROS Measurement. The ROS level within bacteria was tested using the Reactive Oxygen Species Assay Kit (S0033S,

https://doi.org/10.1021/acsami.5c12970
ACS Appl. Mater. Interfaces 2025, 17, 56762–56772

Beyotime Biotechnology Co., Ltd., China), which employed the cell-permeable fluorogenic probe DCFH-DA for the quantitative assay of intracellular levels of ROS in live cells. Then, bacteria were incubated with DCFH-DA for 20 min in the dark and washed with PBS. The intracellular ROS levels were observed with a fluorescence microscope.

Cell Cytotoxicity Tests. Bone marrow mesenchymal stem cells (BMSCs) were seeded into 96-well plates at a density of 5000 cells per well. Fe-TNLs were then immersed in the culture medium and incubated for 1 h. Following this, 100 μL of culture medium was added to each well, and incubation was continued for 24, 48, and 72 h. The culture medium was replaced once daily. After removal of the cell culture medium, 100 μL of a 10% CCK-8 solution (C0038, Beyotime Biotechnology Co., Ltd., China) in medium was added to each well, and the cells were reincubated for 2 h. Absorbance at 450 nm was measured using a microplate reader.

Statistical Analysis. All calculations were performed by using GraphPad Prism 9.5 (GraphPad Software, CA). All data were represented as the mean ± standard deviation. Statistical analysis was performed using Student's *t*-test. A comparison was made between two groups, with a significance level of $^{*}p < 0.05$, $^{**}p < 0.01$, $^{***}p < 0.001$, $^{****}p < 0.0001$, and ns for no significance.

RESULTS

Fabrication and Characterization of Fe-TNLs. The schematic illustration of fabrication for Fe-TNLs is depicted in Scheme 1a. SEM imaging reveals that the synthesized TNLs exhibit diameters of approximately 10 nm and lengths ranging from 100 to 300 nm (Figure 1a). This nanoline morphology is

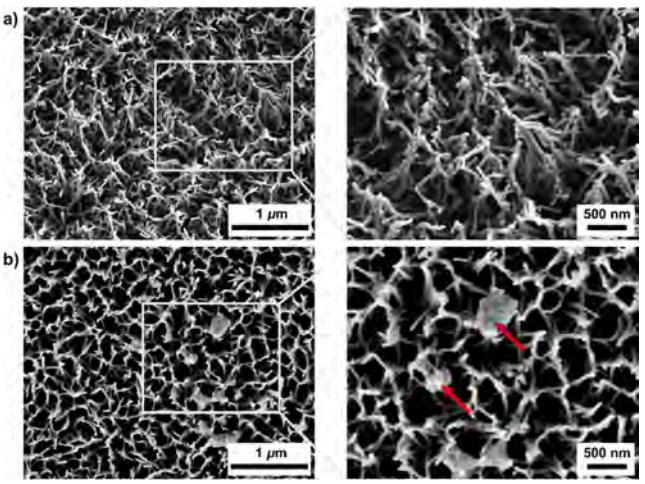

Figure 1. SEM images of TNLs (a) and Fe-TNLs (b) with different magnifications.

anticipated to provide a high surface area, facilitating the attachment of nanozymes.[26] This expectation is validated by the presence of nanoparticles (~50 nm in diameter) observed on the surfaces of the nanolines following ferric chloride treatment (highlighted by red arrows in Figure 1b). EDS mapping further reveals that the distribution of Fe of the particles on Fe-TNLs serves as evidence of the successful fabrication of Fe-TNLs (Figure S1). Fe emission is detected at the sites of the attached nanoparticles, while the remaining regions are predominantly covered with titanium and oxygen elements, indicating effective iron functionalization. This functionalization is expected to exhibit catalytic activity under suitable conditions. As shown in Figure S1, spherical particles with a diameter distribution in the range of 200−300 nm are discerned. EDS analysis demonstrates a pronounced enrichment of the Fe signal in the regions encompassing these particles, suggesting that they represent aggregates of iron oxide. Notably, these iron oxide aggregates constitute a minor fraction of the overall Fe-TNL system. Elemental mapping and quantitative compositional analysis confirm the absence of extraneous impurity elements within these particles, thereby validating their chemical purity. Considering their limited spatial occupancy and uncomplicated chemical composition, these spherical iron oxide particles exert a negligible influence on the properties of Fe-TNLs. The XRD analysis discloses dominant diffraction peaks at 2θ = 27.5° (110), 36.1° (101), and 54.4° (211) from all the samples, indicating the formation of rutile TNLs. The Fe-TNLs demonstrate new peaks at 2θ = 24.1° (012), 33.2° (104), 35.6° (110), and 49.48° (024) of iron oxides, while retaining the remaining titanium dioxide peaks, confirming that the crystallinity is not altered by the doping process (Figure S2).

POD Activity of Fe-TNLs and the Revival Performance under Electrical Stimulation. The pH value is a crucial environmental factor that significantly affects the catalytic activity. Therefore, we tested the POD activity of Fe-TNLs across different pH values to identify the optimal working condition. The Fe-TNLs work best as POD at a pH of 4.5 (Figure S3). Afterward, using a chromogenic assay with 0.1 M TMB in DMSO and 0.1 M H_2O_2, we systematically assessed the POD activity at the optimal pH of 4.5 and substrate concentrations. This method minimizes the impact of pH fluctuations, ensuring that the measured POD activity accurately reflects its true activity. Specifically, the concentration of TMB (1.0 mM) or H_2O_2 (2.0 mM) is fixed, and then the concentration of H_2O_2 (0.05−5 mM, Figure 2a) is varied. To obtain the maximum reaction velocity (V_{max}) and substrate affinity (K_m), the typical double-reciprocal plots ($1/V$ vs $1/[S]$, where "S" represents the substrate concentration) are constructed and fitted to the Michaelis−Menten equation (Figure 2b). Simultaneously, the V_{max} and K_m of varying concentrations of TMB (0.05−1 mM) and a certain concentration of H_2O_2 (2.0 mM) are also measured (Figure 2c,d). After reacting with an unused group under H_2O_2 for 5 min (blue line in Figure 2e), characteristic absorption peaks at 652 nm emerge, which confirms that Fe-TNLs can catalyze the decomposition of H_2O_2, producing ROS and oxidizing TMB. However, the catalytic activity is significantly attenuated after the first catalytic reaction, as evidenced by the decreased absorption intensity in the used group (purple line in Figure 2e). The deactivation of the enzymatic activity is further quantitatively demonstrated by a decrease in the absorbance at 652 nm from 0.79 for the unused sample to 0.30 for the used sample (Figure 2f).

The sample used is then subjected to electrical charging at the working electrode of the three-electrode electrochemical station. The charging time (15 min) and voltage (1.5 V) are chosen based on our preliminary experiment and previous research.[28] The cyclic voltammetry of Fe-TNLs is also shown in Figure S4. The CV characterization of the samples revealed the absence of well-defined redox peaks throughout the electrochemical scans. Nevertheless, discernible disparities in electrochemical reactivity were evidenced, which can be attributed to structural and morphological heterogeneities on the sample surfaces.[29] Specifically, a subtle yet discernible fluctuation is observed at an applied potential of 0.2 V, a finding that implicates the occurrence of redox-mediated valence state transitions within the investigated materials.[30]

https://doi.org/10.1021/acsami.5c12970
ACS Appl. Mater. Interfaces 2025, 17, 56762−56772

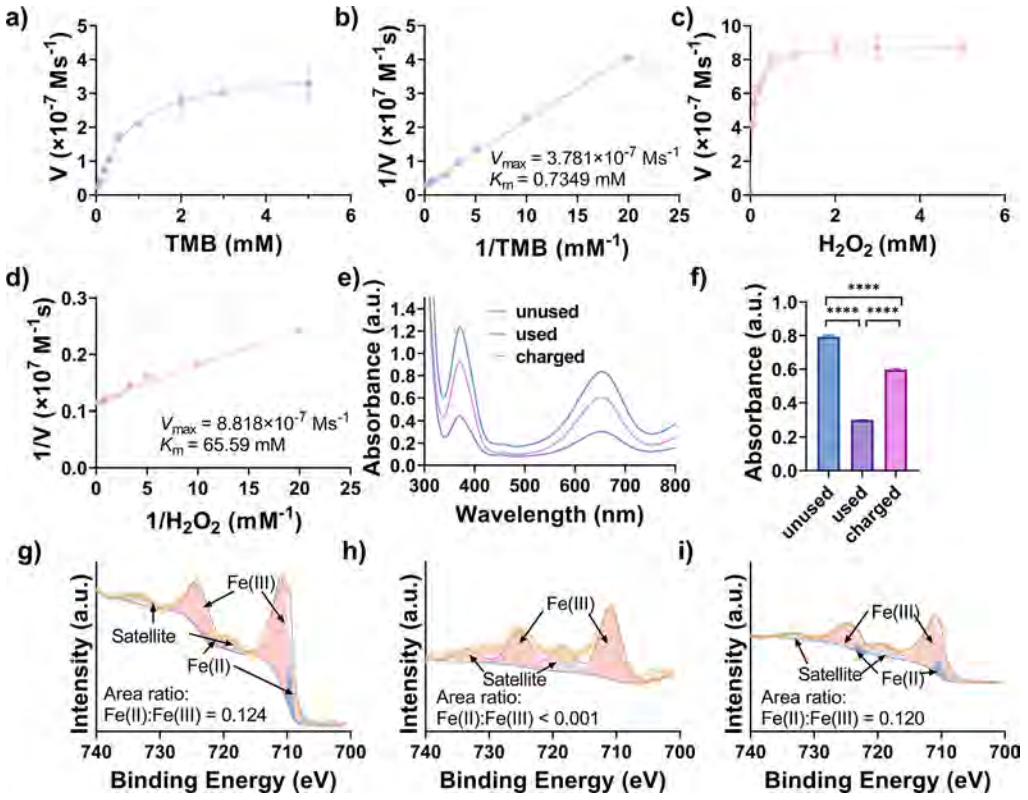

Figure 2. POD activity and elemental change of samples under different treatments. Reaction kinetic assay utilizing the Michaelis−Menten model by varying (a) the H_2O_2 concentration at a fixed TMB concentration (2.0 mM) and (b) changing the TMB concentration at a fixed H_2O_2 concentration (2.0 mM); the double-reciprocal plots of the enzymatic activity of Fe-TNLs for the (c) H_2O_2 and (d) TMB systems; (e) UV−vis spectra of the TMB oxidation products qualitatively demonstrating the POD activity of various samples, with characteristic absorption peaks observed at 370 and 652 nm; (f) quantitative comparison of POD for samples subjected to different treatments; Fe 2p XPS spectra of (g) Fe-TNLs before H_2O_2 exposure (unused group), (h) Fe-TNLs treated by H_2O_2 for 15 min (used group), and (i) after 15 min charging on an electrochemical workstation (charged group).

After charging treatment, the sample, which is marked as a charged group, can again catalyze the decomposition of H_2O_2, generating TMB oxidized products as shown in the pink line in Figure 2e. Although the charging treatment cannot 100% revive the enzyme, the charged sample holds an enzymic activity of the pristine Fe-TNLs partially due to the detachment of Fe from the surface.[31] The decreased POD activity and its revival after charging can also be significantly read by the naked eye (Figure S5).

To investigate whether electrical stimulation damages the structure of Fe-TNLs, XRD analysis is performed. The results show that the rutile-type TNL crystal structure and iron oxide diffraction peaks of the materials in the used and charged groups do not change (Figure S6), confirming that the crystallinity is not altered during the electrical stimulation process.

In order to examine the chemical change in different groups, the elemental species on the surface of Fe-TNLs are analyzed by XPS (Figure S7). As shown in Figure S7a, the binding energy peaks at 710.3 and 723.5 eV are attributed to Fe(II), while the binding energy peaks at 711 and 724.2 eV are attributed to Fe(III).[32−36] Meanwhile, the peaks at 284.8, 286.1, and 288.3 eV are attributed to the C−C, C−O−C, and O−C═O, respectively (Figure S7b).[37] Besides, the peaks at 529.8 and 531.3 eV are attributed to O═O and Ti−O, respectively (Figure S7c).[38,39] Ti−O can also be read from the peaks at 458.6 and 464.3 eV (Figure S7d).[40] The presence of the peaks of O and Ti in the XPS pattern further confirms the formation of TiO_2. The used group (Figure S8a) exhibits no displacement of the C elemental peaks (Figure S8b), the O elemental peaks (Figure S8c), and the Ti elemental peaks (Figure S8d), thereby substantiating the stability of the underlying TiO_2 under the reaction conditions and providing substantiation for its reuse. Meanwhile, the XPS images of the charged group (Figure S9a) resemble those of the unused group. The absence of displacement of the carbon peaks (Figure S9b), oxygen peaks (Figure S9c), and titanium peaks (Figure S9d) proves that applying potential to Fe-TNLs does not alter its chemical structure or elemental valence states.

The deconvolution of Fe 2p XPS spectra confirms the presence of surface Fe(II) species, with an initial Fe(II)/Fe(III) ratio of 0.124:1 in the unused group (Figure 2g). After 15 min of H_2O_2 exposure, Fe(II) signals nearly vanish and turn into Fe(III) (Figure 2h), confirming that the POD activity primarily originates from Fe(II). After charging for 15 min, the ratio of Fe(II)/Fe(III) rises to 0.120:1 (Figure 2i), which proves that the charging process effectively regenerates Fe(II), thereby restoring the POD activity.

To investigate the cause of their inability to recover their full activity, ICP−OES measurements are performed on their leachate. The Fe content in the leachate is measured at 15, 30, and 45 min, with the Fe concentration increasing from 0.146 to 0.21 $\mu g\ L^{-1}$ over time. This suggests that the reduction in the catalytic activity is due to Fe loss (Figure S10).

The Underlying Mechanism for the Electrically Stimulated Revival of Enzymic Activity. To investigate

https://doi.org/10.1021/acsami.5c12970
ACS Appl. Mater. Interfaces 2025, 17, 56762−56772

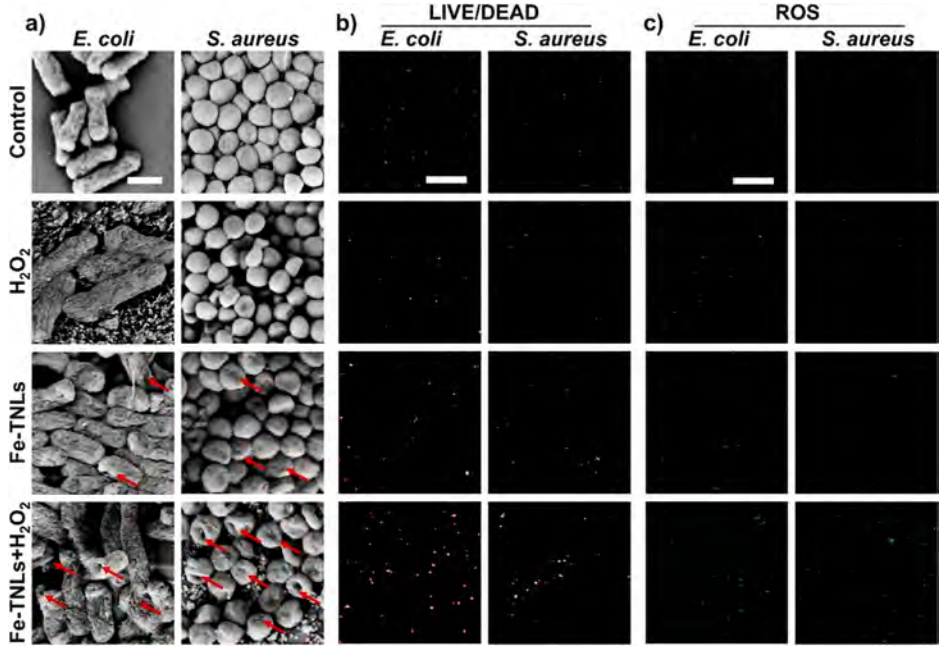

Figure 3. Bactericidal properties of Fe-TNLs based on POD-like activity. (a) SEM images of bacterial morphology (scale bars: 1 μm); (b) live/dead fluorescence staining; and (c) intracellular ROS fluorescence intensity of *E. coli* and *S. aureus* (scale bars: 10 μm).

the mechanisms underlying ROS-related effects, Fe-TNLs and H_2O_2 were analyzed by using electron spin resonance (ESR) to identify the types of ROS produced. As shown in Figure S11, the reaction between Fe-TNLs and H_2O_2 primarily generates $^{\bullet}OH$.[41] It is important to note that superoxide anions ($O_2^{\bullet-}$) were also detected, with their formation being attributed to the reaction between free iron ions and oxygen. However, $^{\bullet}OH$ remains the dominant reactive species, with its signal intensity approximately four times greater than that of $O_2^{\bullet-}$.[42]

Previous studies have demonstrated that electrical polarization of metallic nanostructures can generate ROS and reactive chlorine species (RCS) via Fenton-like reactions.[43] Here, the Fe-TNLs exhibit intrinsic POD-like activity, enabling catalytic decomposition of H_2O_2 into $^{\bullet}OH$ for oxidative degradation of organic pollutants, as described by eqs 1 and 2

$$H_2O_2 + Fe(II) \rightarrow {}^{\cdot}OH + Fe(III) \quad (1)$$

$${}^{\cdot}OH + RH \rightarrow {}^{\cdot}R + H_2O \quad (2)$$

As the most reactive and destructive ROS in biological systems,[44] $^{\bullet}OH$ effectively inactivates bacterial cells in wastewater. Subsequently, Fe(III) generated via the Fenton reaction or pre-existing in the medium can be regenerated into Fe(II) through multiple pathways (eqs 3−5)

$$Fe(III) + H_2O_2 \rightarrow Fe(II) + {}^{\cdot}HO_2 + H^+ \quad (3)$$

$$Fe(III) + {}^{\cdot}HO_2 \rightarrow Fe(II) + O_2 + H^+ \quad (4)$$

$$Fe(III) + {}^{\cdot}R \rightarrow Fe(II) + R^+ \quad (5)$$

However, conventional Fenton systems face limitations due to inefficient Fe(II) recovery and slow regeneration kinetics, leading to gradual POD activity loss over the reaction cycles. To address this, Fe-TNLs are subjected to cyclic voltammetry (CV) charging, facilitating the reduction of Fe(III) to Fe(II) (eq 6)

$$Fe(III) + e^- \rightarrow Fe(II) \quad (6)$$

Based on the above analysis, the revival mechanism for the POD activity can be schematically illustrated in Scheme 1b.

Antibacterial Efficiency Arising from Pristine and Revival POD Activity. Pathogenic bacteria, exemplified by the Gram-negative *E. coli* and Gram-positive *S. aureus*, impose significant public health and socioeconomic burdens due to their aggressive pathogenicity and ubiquitous presence in environmental and clinical settings.[45,46] The POD activity of Fe-TNLs effectively enables antibacterial action by generating ROS through H_2O_2 decomposition, which disrupts pathogenic bacterial cells. To validate its bactericidal potential, in vitro experiments against *E. coli* and *S. aureus* are conducted. Antibacterial efficiency calculated by the cfu counting method shows that the H_2O_2 group has no antibacterial activity, the Fe-TNLs group eliminates 10−20% of the bacteria, and Fe-TNLs kill over 99.99% of *E. coli* and *S. aureus*, exhibiting a universal antibacterial ability. The antibacterial rates of different groups are listed in Table S1. The bacteria treated by different samples are first observed under SEM to qualify the morphological change (Figure 3a). Bacteria on pristine Fe-TNLs exhibit surface deformations and minor pores (red arrows in Figure 3a) due to the mechanical stress from nanoline morphology, while the control group (PBS-treated) maintains intact membranes. The addition of H_2O_2 further exacerbates membrane damage, causing extensive pore formation (red arrows in Figure S12). The changed membrane and distorted morphology indicate that bacteria are under stress, leading to the loss of bacterial viability or even death.[47]

The viability of bacteria is then evaluated by live and dead staining (Figure 3b). The untreated bacteria show strong green fluorescence (viable cells), whereas the Fe-TNLs + H_2O_2 group displays predominant red fluorescence (dead cells), outperforming both the control and H_2O_2-only groups. Pristine Fe-TNLs alone induce partial cell death (mixed red/green fluorescence), indicating their limited standalone efficacy. Furthermore, elevated intracellular ROS fluorescence intensity in the Fe-TNLs + H_2O_2 group (Figure 3c) confirms

https://doi.org/10.1021/acsami.5c12970
ACS Appl. Mater. Interfaces 2025, 17, 56762−56772

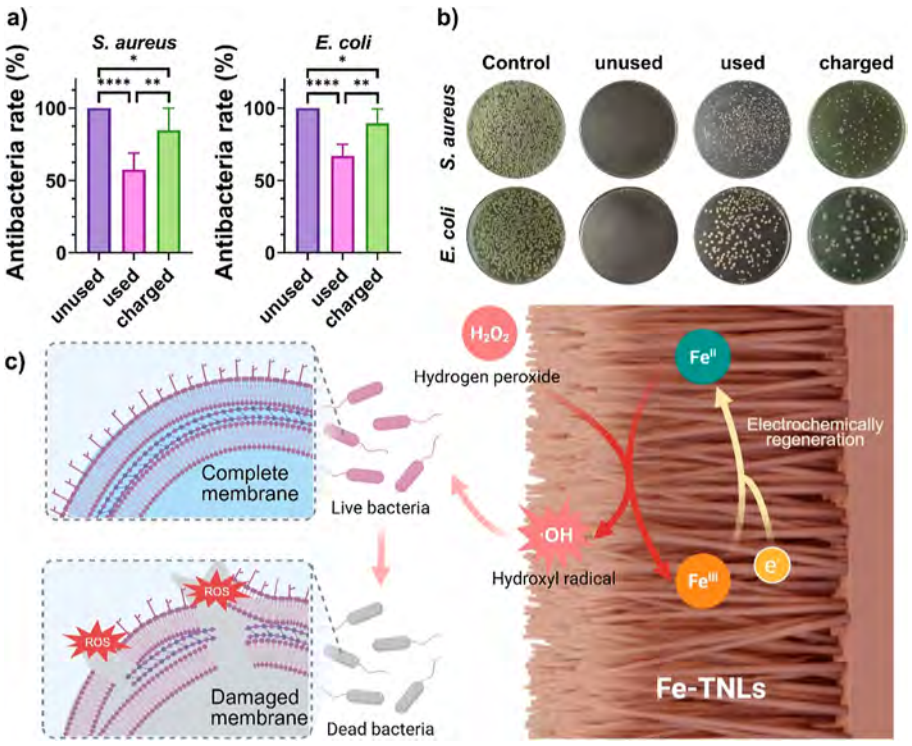

Figure 4. Restoration of sterilizing properties. (a) Statistical analysis of antibacterial efficiency and (b) colony counting results of *E. coli* and *S. aureus* after sequential antibacterial cycles; (c) mechanistic diagram illustrating the H_2O_2 decomposition into hydroxyl radicals ($^{\bullet}OH$) by Fe-TNLs' POD-like activity, inducing oxidative damage and bacterial inactivation.

that the POD-like activity amplifies oxidative stress, directly linked to bacterial membrane rupture. As depicted in Figure 3c, the catalytic generation of $^{\bullet}OH$ by Fe-TNLs triggers oxidative damage, compromising membrane integrity and leading to cell lysis.[48−50] This mechanism underscores that Fe-TNLs with POD activity could work synergistically with H_2O_2 to achieve efficient and sustainable bacterial inactivation, with implications for wastewater treatment and antimicrobial material design.

Furthermore, to ascertain whether the leached Fe is detrimental to humans or animals, BMSCs were cocultured with the leachate, and the resulting cellular toxicity was characterized using the CCK-8 assay. The findings indicated that while the leachate contains Fe, it does not exert a substantial impact on BMSCs. The growth rate of cells in the Fe-TNLs group is found to be approximately 90% of that observed in the pure culture medium group (Figure S13). In practical applications, Fe-TNLs would be applied directly to environmental wastewater and do not come into prolonged contact with the human body, ensuring their safety during use.

Restoration of Antibacterial Performance in Fe-TNLs. As demonstrated in Figure 4a,b, although pristine Fe-TNLs exhibit exceptional antibacterial activity (99.9%) in the first cycle, their efficacy drops significantly to 55% for *E. coli* and 60% for *S. aureus* (used group), primarily due to the exhaustion of POD-like activity. In the context of wastewater treatment, this decline may lead to considerable resource wastage and pose a risk of secondary pollution, which underscores the significance of enzymic activity revival by charging. To demonstrate that electrical stimulation charging restores the POD-like activity of Fe-TNLs and consequently regenerates its antibacterial efficacy, a three-stage antibacterial experiment was conducted. Following electrical stimulation reactivation (charging treatment), the antibacterial efficiency of Fe-TNLs recovers to approximately 80% for both strains (charged group), consistent with the restoration of its POD-like activity (Figure 2f). Building on these results, we propose the restored antibacterial mechanism, as shown in Figure 4c. As previously described, the POD-like activity of Fe-TNLs enables the catalytic decomposition of H_2O_2 into $^{\bullet}OH$, which effectively inactivates bacterial cells through oxidative damage. The oxidative stress triggers uncontrolled accumulation of ROS and kills bacteria by inducing membrane disruption, protein dysfunction, and genetic damage. These results conclusively link the reactivation of POD-like activity to the regeneration of Fe-TNLs' antibacterial function, validating its potential for cyclic use in antimicrobial applications (Scheme 1c).

Enzyme Revival to Enhance Antibacterial Efficacy in Simulated Wastewater. To validate the bactericidal efficacy of Fe-TNLs in environmental wastewater, we investigate their performance in simulated bacterial-contaminated wastewater. The synthetic wastewater is prepared according to the Organization for Economic Co-operation and Development standard guidelines (composition detailed in Table S2).[51]

E. coli is introduced into the synthetic wastewater to achieve a final bacterial concentration of 10^5 cfu mL^{-1}. Antibacterial experiments and colony counting are performed as described earlier. Results demonstrate that Fe-TNLs achieve an 80−90% bacterial inactivation efficiency during the first treatment cycle, comparable to their performance in pure bacterial suspensions. However, the efficiency drops to ∼40% upon usage, while electrical reactivation restores the activity to ∼60%, confirming the revival of enzymic activity for Fe-TNLs (Figures S14 and S15). In simulated wastewater environments, various organic substances are commonly present as impurities. Consequently, the antimicrobial efficiency of ROS-based treatments is

https://doi.org/10.1021/acsami.5c12970
ACS Appl. Mater. Interfaces 2025, 17, 56762−56772

significantly diminished in the presence of such organic contaminants.[52] These findings underscore the potential of rechargeable Fe-TNLs for practical applications in complex wastewater systems, highlighting their practical applicability in real-world bacterial decontamination scenarios.

DISCUSSION

The irreversible deactivation in conventional enzyme-like materials has long hindered their practical application. Although a few researchers have tried to enhance the enzymic activity by increasing the loading of active sites,[53] or designing the composition of the active sites,[25] they still suffer from the high cost and complexity of the process. The use of reductants has been explored to facilitate the conversion of high-valent to low-valent transition metal species, thereby restoring the enzymatic activity. However, this approach introduces unavoidable environmental challenges, particularly since the restoration process often involves high energy consumption and the use of toxic substances.[54−56] Although less polluting chemical reductants, such as ascorbate, are employed due to their relatively lower environmental impact, they still result in high operational costs. In catalytic processes, the amount of ascorbic acid required is often equivalent to that of the catalyst itself to restore or enhance activity.[57,58] This is mainly due to their stoichiometric consumption in each reactivation cycle,[59] along with the additional expenses related to waste management for treating residual reductants and byproducts. In contrast, electrical reactivation, while requiring an initial investment in equipment such as electrodes and power sources, eliminates the need for consumables, thereby resulting in lower long-term costs. Furthermore, electrical stimulation offers significant advantages over chemical reductants, including greater cost efficiency, reduced environmental impact, and the potential for more sustainable operations in the long term. It has been reported that the use of photothermal methods can precisely control the antibacterial properties of materials,[60] but there are few reports on methods for restoring activity through electrical stimulation.

In this work, the development of Fe-TNLs as rechargeable enzyme-mimetic catalysts represents a possible way to address the above limitation. By application of a low voltage to Fe-TNLs, Fe(III) undergoes electrical reduction to Fe(II) at the electrode surface. This ionic transformation enables a cyclic mechanism as follows:

(1) Fe(II) reacts with H_2O_2 to generate $^{\bullet}OH$, concomitantly oxidizing to Fe(III);
(2) The generated $^{\bullet}OH$ radicals oxidize bacterial contaminants in wastewater;
(3) Fe(III) is reduced back to Fe(II) via applied voltage;
(4) The regenerated Fe(II) reinitiates the catalytic sequence, establishing a self-sustaining redox loop.

The ability to restore over 80% of the initial catalytic activity through simple electrical charging marks a departure from traditional systems reliant on chemical reductants or disposable catalysts, offering a scalable and energy-efficient alternative. Compared to reagent-driven Fenton processes, the electrical approach eliminates secondary pollution from unused oxidants or metal sludge.[61,62] This system features operational simplicity and robust cyclability, with its POD-like activity being electrochemically restored upon application of the optimized voltage. The electrical reversibility between Fe(II) and Fe(III) has been well established in battery-related studies,[63−65] highlighting its potential for high-efficiency resource utilization through repeated charge−discharge cycles in sustainable catalytic systems. This reversible redox cycle also shows great promise for scalable water decontamination applications, warranting further investigation into its effectiveness against a broad range of aqueous pollutants.

The structural advantages of the TNLs carrier further distinguish Fe-TNLs from existing nanomaterials. Beyond the intrinsic antibacterial activity induced by mechanical stress from the nanolined architecture (Figure 3a), the high surface area and strong metal−support interactions effectively prevent Fe nanoparticle aggregation and promote close contact with bacterial cells, thereby enhancing oxidative damage through localized $^{\bullet}OH$ generation. As one of the most efficient ROS, $^{\bullet}OH$ can rapidly disrupt microbial membranes, proteins, and DNA, resulting in efficient bacterial inactivation.[8,66] Moreover, $^{\bullet}OH$ can nonselectively oxidize a broad spectrum of organic pollutants, including dyes, pharmaceuticals, phenolic compounds, and other persistent organic contaminants.[67−69] This dual functionality, combining pollutant degradation with pathogen inactivation, positions Fe-TNLs as a multifunctional platform for integrated water remediation. Nonetheless, since the current study primarily targets model pathogens (*E. coli*, *S. aureus*) in synthetic wastewater, further investigations are required to assess the efficacy of the electrical stimulation strategy in more complex contamination scenarios, including industrial effluents and antibiotic-resistant bacterial strains.

One limitation of the current regeneration process is the loss of iron. While the process successfully recovers approximately 80% of the catalytic activity, this recovery is not fully reversible due to the gradual leaching of iron from the catalyst. This iron loss limits the long-term stability and efficiency of the system, as it impacts the catalyst's ability to regenerate its activity over extended use. Further investigations are needed to minimize iron loss and improve the durability of the catalyst in order to achieve more consistent and sustainable regeneration.

CONCLUSION

Given the irreversible loss of enzymatic activity after a single use in conventional metal-based enzymes, in this study, we propose an electrically stimulated reactivation strategy to restore the POD-like activity of Fe-TNLs through the establishment of a Fe(III)/Fe(II) redox cycle, thereby enabling sustained antibacterial performance in wastewater treatment. By anchoring Fe nanoparticles onto a high-surface-area TNLs carrier, the composite achieves catalytic decomposition of H_2O_2 into $^{\bullet}OH$ for pathogen inactivation. Notably, by charging the interface for 15 min, Fe(II) could be regenerated from oxidized Fe(III), restoring >80% of the initial POD-like activity and enabling cyclic reuse. Structural characterization and kinetic assays confirm that the TNLs substrate stabilizes Fe nanoparticles while enhancing bacterial contact, synergistically improving bactericidal efficiency. The integration of electrical regeneration with nanoscale engineering resolves the trade-off between catalytic performance and longevity in enzyme-mimetic systems. The revival of enzymic activity is also confirmed in simulated wastewater (60% efficiency postreactivation), underscoring its practical potential for sustainable water treatment. This work represents a paradigm shift from disposable catalysts to rechargeable materials, holding promise for industrial-scale applications and broader catalytic functionalities beyond water remediation.

https://doi.org/10.1021/acsami.5c12970
ACS Appl. Mater. Interfaces 2025, 17, 56762−56772

■ ASSOCIATED CONTENT

Supporting Information

The Supporting Information is available free of charge at https://pubs.acs.org/doi/10.1021/acsami.5c12970.

Antibacterial rates of different groups; Composition details of the synthetic wastewater; EDS mapping images of the Fe-TNLs sample; XRD patterns of the TNLs and Fe-TNLs samples; the influence of pH on the POD-like activity of Fe-TNLs; the cyclic voltammogram of Fe-TNL; POD activity measurement; XRD patterns of unused group, used group and charged group; XPS survey spectrum of Fe-TNLs of unused group, used group, and charged group; concentration of Fe in solution after immersion for different periods; the ESR spectra corresponding to the $^{\bullet}OH$ and $O_2^{\bullet-}$ species in Fe-TNLs and H_2O_2; SEM images of bacteria interacting with Fe-TNLs under the addition of H_2O_2; growth of BMSCs measured by CCK-8 under different culture times in Fe-TNLs leachate; colony counting in antimicrobial experiments on simulated wastewater; and antimicrobial efficiency of samples in simulated wastewater (PDF)

■ AUTHOR INFORMATION

Corresponding Authors

Jianzhong Du − *Department of Gynaecology and Obstetrics, Shanghai Key Laboratory of Anesthesiology and Brain Functional Modulation, Clinical Research Center for Anesthesiology and Perioperative Medicine, Translational Research Institute of Brain and Brain-Like Intelligence, Shanghai Fourth People's Hospital, School of Medicine, Tongji University, Shanghai 200434, China; Key Laboratory of Advanced Civil Engineering Materials of Ministry of Education, School of Materials Science and Engineering, Tongji University, Shanghai 201804, China; School of Materials Science and Engineering, East China University of Science and Technology, Shanghai 200237, China;* orcid.org/0000-0003-1889-5669; Email: jzdu@tongji.edu.cn

Guomin Wang − *State Key Laboratory of Cardiovascular Diseases and Medical Innovation Center, Shanghai East Hospital, Department of Cardiovascular Surgery, Shanghai Tenth People's Hospital, School of Medicine, Tongji University, Shanghai 200040, China;* orcid.org/0000-0003-2707-7051; Email: gwang@tongji.edu.cn

Authors

Jingyang Fang − *Department of Polymeric Materials, School of Materials Science and Engineering, Tongji University, Shanghai 201804, China;* orcid.org/0009-0003-5314-4876

Guopeng Xu − *State Key Laboratory of Cardiovascular Diseases and Medical Innovation Center, Shanghai East Hospital, Department of Cardiovascular Surgery, Shanghai Tenth People's Hospital, School of Medicine, Tongji University, Shanghai 200040, China;* orcid.org/0009-0005-6742-5104

Paul K. Chu − *Department of Physics, Department of Materials Science and Engineering and Department of Biomedical Engineering, City University of Hong Kong, Kowloon, Hong Kong 999077, China;* orcid.org/0000-0002-5581-4883

Complete contact information is available at: https://pubs.acs.org/10.1021/acsami.5c12970

Author Contributions

J.D. and G.W. conceived and directed the project. J.F. and G.X. designed and performed the experiments. G.X. helped with the data analysis. J.F., J.D., and G.W. wrote the paper. All authors discussed the results and commented on the manuscript.

Notes

The authors declare no competing financial interest.

■ ACKNOWLEDGMENTS

This research was supported by the National Key Research and Development Program of China (2023YFB3809900 and 2023YFB3809901), the National Natural Science Foundation of China (82302382 and 22335005), the Shanghai Natural Science Foundation (23ZR1467100), the Innovation Program of Shanghai Municipal Education Commission (2023ZKZD28), and the Fundamental Research Funds for the Central Universities.

■ REFERENCES

(1) Alvarez, P. J. J.; Chan, C. K.; Elimelech, M.; Halas, N. J.; Villagrán, D. Emerging Opportunities for Nanotechnology to Enhance Water Security. *Nat. Nanotechnol.* **2018**, *13*, 634−641.

(2) Liu, Y.-Y.; Wang, Y.; Walsh, T. R.; Yi, L.-X.; Zhang, R.; Spencer, J.; Doi, Y.; Tian, G.; Dong, B.; Huang, X.; Yu, L.-F.; Gu, D.; Ren, H.; Chen, X.; Lv, L.; He, D.; Zhou, H.; Liang, Z.; Liu, J.-H.; Shen, J. Emergence of Plasmid-Mediated Colistin Resistance Mechanism Mcr-1 in Animals and Human Beings in China: A Microbiological and Molecular Biological Study. *Lancet Infect. Dis.* **2016**, *16*, 161−168.

(3) Murray, C. J. L.; Ikuta, K. S.; Sharara, F.; Swetschinski, L.; Robles Aguilar, G.; Gray, A.; Han, C.; Bisignano, C.; Rao, P.; Wool, E.; Johnson, S. C.; Browne, A. J.; Chipeta, M. G.; Fell, F.; Hackett, S.; Haines-Woodhouse, G.; Kashef Hamadani, B. H.; Kumaran, E. A. P.; McManigal, B.; Achalapong, S.; et al. Global Burden of Bacterial Antimicrobial Resistance in 2019: A Systematic Analysis. *Lancet* **2022**, *399*, 629−655.

(4) Rutala, W. A.; Weber, D. J. Best Practices for Disinfection of Noncritical Environmental Surfaces and Equipment in Health Care Facilities: A Bundle Approach. *Am. J. Infect. Control* **2019**, *47*, A96−A105.

(5) He, S.; Chen, Y.; Li, X.; Zeng, L.; Zhu, M. Heterogeneous Photocatalytic Activation of Persulfate for the Removal of Organic Contaminants in Water: A Critical Review. *ACS ES&T Eng.* **2022**, *2*, 527−546.

(6) Liu, Y.; Li, W.; Jin, L.; You, S.; Liu, M. Understanding the Multiple Roles of Electrified Mxene Filter toward Boosting the Fenton-Like Reaction. *Sep. Purif. Technol.* **2024**, *343*, 127092.

(7) Gao, M.; Ren, Y.; Zheng, W.; Liu, M.; Wang, X.; Nanayakkara, N.; Liu, Y. Fine-Tune the Electronic Structure of Single-Atom Pd Via Halogen Doping toward Boosted Fenton-Like Reaction. *Appl. Catal., B* **2025**, *371*, 125218.

(8) Attar, F.; Shahpar, M. G.; Rasti, B.; Sharifi, M.; Saboury, A. A.; Rezayat, S. M.; Falahati, M. Nanozymes with Intrinsic Peroxidase-Like Activities. *J. Mol. Liq.* **2019**, *278*, 130−144.

(9) Dai, M.; Wang, R. Synthesis and Applications of Nanostructured Hollow Transition Metal Chalcogenides. *Small* **2021**, *17*, 2006813.

(10) Jothi, P. R.; Yubuta, K.; Fokwa, B. P. T. A. S. A Simple, General Synthetic Route toward Nanoscale Transition Metal Borides. *Adv. Mater.* **2018**, *30*, 1704181.

(11) Chai, L.; Zaburdaev, V.; Kolter, R. How Bacteria Actively Use Passive Physics to Make Biofilms. *Proc. Natl. Acad. Sci. U.S.A.* **2024**, *121*, No. e2403842121.

(12) Kikani, B.; Patel, R.; Thumar, J.; Bhatt, H.; Rathore, D. S.; Koladiya, G. A.; Singh, S. P. Solvent Tolerant Enzymes in

Extremophiles: Adaptations and Applications. *Int. J. Biol. Macromol.* **2023**, *238*, 124051.
(13) Zhang, Y.; Hess, H. Microenvironmental Engineering: An Effective Strategy for Tailoring Enzymatic Activities. *Chin. J. Chem. Eng.* **2020**, *28*, 2028−2036.
(14) Kumar, P.; Kermanshahi-Pour, A.; Brar, S. K.; He, Q. S.; Rainey, J. K. Influence of Elevated Pressure and Pressurized Fluids on Microenvironment and Activity of Enzymes. *Biotechnol. Adv.* **2023**, *68*, 108219.
(15) Mohidem, N. A.; Mohamad, M.; Rashid, M. U.; Norizan, M. N.; Hamzah, F.; Mat, H. b. Recent Advances in Enzyme Immobilisation Strategies: An Overview of Techniques and Composite Carriers. *J. Compos. Sci.* **2023**, *7*, 488.
(16) Darwesh, O. M.; Matter, I. A.; Eida, M. F. Development of Peroxidase Enzyme Immobilized Magnetic Nanoparticles for Bioremediation of Textile Wastewater Dye. *J. Environ. Chem. Eng.* **2019**, *7*, 102805.
(17) Kim, S. H.; Kim, K.-R.; Ahn, D.-R.; Lee, J. E.; Yang, E. G.; Kim, S. Y. Reversible Regulation of Enzyme Activity by Ph-Responsive Encapsulation in DNA Nanocages. *ACS Nano* **2017**, *11*, 9352−9359.
(18) Wang, F.; Liu, Y.; Du, C.; Gao, R. Current Strategies for Real-Time Enzyme Activation. *Biomolecules* **2022**, *12*, 599.
(19) Ye, S.; Chen, S.; Cai, T.; Sheng, R.; Peng, H. Iron-Driven Self-Assembly of Dopamine into Dumbbell-Shaped Nanozyme for Visual and Rapid Detection of Norfloxacin on a Smartphone-Assisted Platform. *Talanta* **2024**, *274*, 126003.
(20) Zhang, Q.; Zhou, M.; Du, X.; Su, P.; Fu, W.; Song, G. Highly Efficient Dual-Cathode Electro-Fenton Process without Aeration at a Wide Ph Range: Simultaneously Enhancing Fe(Ii) Regeneration and Mineralization Efficiency. *Chem. Eng. J.* **2022**, *429*, 132436.
(21) Gu, Z.; Zhong, D.; Hou, X.; Wei, X.; Liu, C.; Zhang, Y.; Duan, Z.; Gu, Z.; Gong, Q.; Luo, K. Unraveling Ros Conversion through Enhanced Enzyme-Like Activity with Copper-Doped Cerium Oxide for Tumor Nanocatalytic Therapy. *Adv. Sci.* **2024**, *11*, 2307154.
(22) Wei, S.; Zhang, W.; Wang, Z.; Zhang, G.; Li, W.-W.; Zeng, G.; Zhang, S. Operando Surface Ligands Boost Pt Nanozyme Activity for H_2O_2 Catalysis Via Bridged Electron Transfer. *ACS Catal.* **2025**, *15*, 6439−6449.
(23) Zhu, X.; Xiong, C.; Zhou, H.; Wang, J.; Wu, Y. Single-Atom Nanozymes for Enhanced Electrochemical Biosensing: A Review. *Talanta* **2025**, *294*, 128179.
(24) Song, G.; Zhang, Z.; Fauconnier, M.-L.; Li, C.; Chen, L.; Zheng, X.; Zhang, D. Bimodal Single-Atom Iron Nanozyme Biosensor for Volatile Amine and Food Freshness Detection. *Nano Today* **2023**, *53*, 102025.
(25) Xie, J.; Li, S.; Zhang, C.; Jing, J.; Liu, J.; Zhou, M. Insights into Transition Metal Encapsulated inside Carbon Aerogel for Accelerated Electro-Peroxone Oxidation: Activity Evaluation and Reactive Oxygen Species Generation. *Chem. Eng. J.* **2024**, *498*, 155706.
(26) Wang, G.; Feng, H.; Hu, L.; Jin, W.; Hao, Q.; Gao, A.; Peng, X.; Li, W.; Wong, K.-Y.; Wang, H.; Li, Z.; Chu, P. K. An Antibacterial Platform Based on Capacitive Carbon-Doped TiO_2 Nanotubes after Direct or Alternating Current charging. *Nat. Commun.* **2018**, *9*, 2055.
(27) Lemire, J. A.; Harrison, J. J.; Turner, R. J. Antimicrobial Activity of Metals: Mechanisms, Molecular Targets and Applications. *Nat. Rev. Microbiol.* **2013**, *11*, 371−384.
(28) Zhang, L.; Kepp, K. P.; Ulstrup, J.; Zhang, J. Redox Potentials and Electronic States of Iron Porphyrin Ix Adsorbed on Single Crystal Gold Electrode Surfaces. *Langmuir* **2018**, *34*, 3610−3618.
(29) Roberts, J. J. P.; Westgard, J. A.; Cooper, L. M.; Murray, R. W. Solution Voltammetry of 4 Nm Magnetite Iron Oxide Nanoparticles. *J. Am. Chem. Soc.* **2014**, *136*, 10783−10789.
(30) Bülter, H.; Denuault, G.; Mátéfi-Tempfli, S.; Mátéfi-Tempfli, M.; Dosche, C.; Wittstock, G. Electrochemical Analysis of Nano-structured Iron Oxides Using Cyclic Voltammetry and Scanning Electrochemical Microscopy. *Electrochim. Acta* **2016**, *222*, 1326−1334.
(31) Dong, H.; Du, W.; Dong, J.; Che, R.; Kong, F.; Cheng, W.; Ma, M.; Gu, N.; Zhang, Y. Depletable Peroxidase-Like Activity of Fe3o4 Nanozymes Accompanied with Separate Migration of Electrons and Iron Ions. *Nat. Commun.* **2022**, *13*, 5365.
(32) Tan, B. J.; Klabunde, K. J.; Sherwood, P. M. A. X-Ray Photoelectron Spectroscopy Studies of Solvated Metal Atom Dispersed Catalysts. Monometallic Iron and Bimetallic Iron-Cobalt Particles on Alumina. *Chem. Mater.* **1990**, *2*, 186−191.
(33) Mu, Y.; Jia, F.; Ai, Z.; Zhang, L. Iron Oxide Shell Mediated Environmental Remediation Properties of Nano Zero-Valent Iron. *Environ. Sci.: Nano* **2017**, *4*, 27−45.
(34) Fu, J.; Li, T.; Yang, Y.; Jiang, L.; Wang, W.; Fu, L.; Zhu, Y.; Hao, Y. Activatable Nanomedicine for Overcoming Hypoxia-Induced Resistance to Chemotherapy and Inhibiting Tumor Growth by Inducing Collaborative Apoptosis and Ferroptosis in Solid Tumors. *Biomaterials* **2021**, *268*, 120537.
(35) Perco, D.; Loi, F.; Bignardi, L.; Sbuelz, L.; Lacovig, P.; Tosi, E.; Lizzit, S.; Kartouzian, A.; Heiz, U.; Baraldi, A. The Highest Oxidation State Observed in Graphene-Supported Sub-Nanometer Iron Oxide Clusters. *Commun. Chem.* **2023**, *6*, 61.
(36) Qing, Z.-L.; Hu, H.; Mi, J.-L.; Qi, F.-M.; Li, J.-L.; Song, J.-D.; Xiao, B.-B.; Yong, Y.-C. Cofe-(Oxy)Hydroxide@Co_3O_4-CeO_2 Core−Shell Nanorods on Nickel Foam for Oxygen Evolution Reaction. *ACS Appl. Nano Mater.* **2024**, *7*, 20370−20379.
(37) Chen, Z.; Chen, H.; Wang, K.; Chen, J.; Li, M.; Wang, Y.; Tsiakaras, P.; Song, S. Enhanced TiO_2 Photocatalytic 2 E− Oxygen Reduction Reaction Via Interfacial Microenvironment Regulation and Mechanism Analysis. *ACS Catal.* **2023**, *13*, 6497−6508.
(38) Xie, Q.; Jiang, M.; Kong, H.; Huang, Q.; Wu, C.; Wang, Y.; Chen, Y.; Li, H.; Yan, Y. Enhanced Air-Poisoning Resistance in Vanadium-Based Hydrogen Storage Alloy by Addition of Si. *Prog. Nat. Sci.: Mater. Int.* **2024**, *34*, 648−653.
(39) Duan, Y.; Zhang, M.; Wang, L.; Wang, F.; Yang, L.; Li, X.; Wang, C. Plasmonic Ag-TiO_2−X Nanocomposites for the Photo-catalytic Removal of No under Visible Light with High Selectivity: The Role of Oxygen Vacancies. *Appl. Catal., B* **2017**, *204*, 67−77.
(40) Chadwick, N. P.; Kafizas, A.; Quesada-Cabrera, R.; Sotelo-Vazquez, C.; Bawaked, S. M.; Mokhtar, M.; Al Thabaiti, S. A.; Obaid, A. Y.; Basahel, S. N.; Durrant, J. R.; Carmalt, C. J.; Parkin, I. P. Ultraviolet Radiation Induced Dopant Loss in a TiO_2 Photocatalyst. *ACS Catal.* **2017**, *7*, 1485−1490.
(41) Jiang, B.; Duan, D.; Gao, L.; Zhou, M.; Fan, K.; Tang, Y.; Xi, J.; Bi, Y.; Tong, Z.; Gao, G. F.; Xie, N.; Tang, A.; Nie, G.; Liang, M.; Yan, X. Standardized Assays for Determining the Catalytic Activity and Kinetics of Peroxidase-Like Nanozymes. *Nat. Protoc.* **2018**, *13*, 1506−1520.
(42) Kimura, M.; Kawano, T. Hydrogen Peroxide-Independent Generation of Superoxide Catalyzed by Soybean Peroxidase in Response to Ferrous Ion. *Plant Signaling Behav.* **2015**, *10*, No. e1010917.
(43) Vargas-Lizarazo, A. Y.; Ali, M. A.; Mazumder, N. A.; Kohli, G. M.; Zaborska, M.; Sons, T.; Garnett, M.; Senanayake, I. M.; Goodson, B. M.; Vargas-Muñiz, J. M.; Pond, A.; Jensik, P. J.; Olson, M. E.; Hamilton-Brehm, S. D.; Kohli, P. Electrically Polarized Nanoscale Surfaces Generate Reactive Oxygenated and Chlorinated Species for Deactivation of Microorganisms. *Sci. Adv.* **2024**, *10*, No. eado5555.
(44) Buettner, G. R. The Pecking Order of Free Radicals and Antioxidants: Lipid Peroxidation, A-Tocopherol, and Ascorbate. *Arch. Biochem. Biophys.* **1993**, *300*, 535−543.
(45) Li, R. S.; Liu, J.; Wen, C.; Shi, Y.; Ling, J.; Cao, Q.; Wang, L.; Shi, H.; Huang, C. Z.; Li, N. Transformable Nano-Antibiotics for Mechanotherapy and Immune Activation against Drug-Resistant Gram-Negative Bacteria. *Sci. Adv.* **2023**, *9*, No. eadg9601.
(46) Zhang, Z.; Wang, X.; Liu, J.; Yang, H.; Tang, H.; Li, J.; Luan, S.; Yin, J.; Wang, L.; Shi, H. Structural Element of Vitamin U-Mimicking Antibacterial Polypeptide with Ultrahigh Selectivity for Effectively Treating Mrsa Infections. *Angew. Chem., Int. Ed.* **2024**, *63*, No. e202318011.
(47) Bose, S.; Dahat, Y.; Kumar, D.; Haldar, S.; Das, S. K. A Membrane Targeted Multifunctional Cationic Nanoparticle Conjugated Fusogenic Nanoemulsion (Cfuson): Induced Membrane

Depolarization and Lipid Solubilization to Accelerate the Killing of Staphylococcus Aureus. *Mater. Horiz.* **2024**, *11*, 661−679.
(48) Lin, C.; Guo, X.; Chen, L.; You, T.; Lu, J.; Sun, D. Ultrathin Trimetallic Metal−Organic Framework Nanosheets for Accelerating Bacteria-Infected Wound Healing. *J. Colloid Interface Sci.* **2022**, *628*, 731−744.
(49) Lin, T.; Jiang, G.; Lin, D.; Lai, Y.; Hou, L.; Zhao, S. Bacitracin-Functionalized Dextran-Mose2 with Peroxidase-Like and near-Infrared Photothermal Activities for Low-Temperature and Synergetic Antibacterial Applications. *ACS Appl. Bio Mater.* **2022**, *5*, 2347−2354.
(50) Yuan, G.; Zhang, S.; Yang, Z.; Wu, S.; Chen, H.; Tian, X.; Cheng, S.; Pan, Y.; Zhou, R. Precisely Modulated 2d Pdcu Alloy Nanodendrites as Highly Active Peroxidase Mimics for the Elimination of Biofilms. *Biomater. Sci.* **2022**, *10*, 7067−7076.
(51) OECD *Test No. 303: Simulation Test-Aerobic Sewage Treatment-A: Activated Sludge Units; B: Biofilms*; OECD Publishing: Paris, 2001.
(52) Lopes, J.; Marques-da-Silva, D.; Peralta, C.; Rodrigues, J. R.; Vaz, D.; Lagoa, R. Humic Acid Aggregates with Laccase and Decreases the Performance of the Enzyme Catalytic Systems through Various Mechanisms. *Int. J. Biol. Macromol.* **2025**, *322*, 146405.
(53) Chen, S.; Huang, F.; Mao, L.; Zhang, Z.; Lin, H.; Yan, Q.; Lu, X.; Shi, J. High Fe-Loading Single-Atom Catalyst Boosts Ros Production by Density Effect for Efficient Antibacterial Therapy. *Nano-Micro Lett.* **2024**, *17*, 32.
(54) Zhou, C.; Zhou, P.; Sun, M.; Liu, Y.; Zhang, H.; Xiong, Z.; Liang, J.; Duan, X.; Lai, B. Nitrogen-Doped Carbon Nanotubes Enhanced Fenton Chemistry: Role of near-Free Iron(III) for Sustainable Iron(III)/Iron(II) Cycles. *Water Res.* **2022**, *210*, 117984.
(55) Song, H.; Zu, D.; Li, C.; Zhou, R.; Wang, Y.; Zhang, W.; Pan, S.; Cai, Y.; Li, Z.; Shen, Y.; Ma, J. Ultrafast Activation of Peroxymonosulfate by Reduction of Trace Fe^{3+} with Ti_3C_2 Mxene under Neutral and Alkaline Conditions: Reducibility and Confinement Effect. *Chem. Eng. J.* **2021**, *423*, 130012.
(56) Shi, X.; Li, Y.; Zhang, Z.; Sun, L.; Peng, Y. Enhancement of Ciprofloxacin Degradation in the Fe(Ii)/Peroxymonosulfate System by Protocatechuic Acid over a Wide Initial Ph Range. *Chem. Eng. J.* **2019**, *372*, 1113−1121.
(57) Ramos, M. D. N.; Silva, G. L. S.; Lessa, T. L.; Aguiar, A. Study of Kinetic Parameters Related to Dyes Oxidation in Ascorbic Acid-Mediated Fenton Processes. *Process Saf. Environ. Prot.* **2022**, *168*, 1131−1141.
(58) Bolobajev, J.; Trapido, M.; Goi, A. Improvement in Iron Activation Ability of Alachlor Fenton-Like Oxidation by Ascorbic Acid. *Chem. Eng. J.* **2015**, *281*, 566−574.
(59) Zu, D.; Liu, J.; Wei, H.; Yang, K.; Tian, H.; Ma, J.; Yang, Z. Comparative Life Cycle Assessment of Fenton-Like Systems: Insights into the Environmental Benefits of Reductant-Driven Strategies. *Water Res.* **2025**, *279*, 123489.
(60) He, X.; Wu, H.; Xu, K.; Tang, J.; Li, C.; Sathishkumar, G.; Rao, X.; Murugesan, S.; Barão, V. A. R.; Kang, E.-T.; Xu, L. Biomimetic Engineering of Robust Gradient Antibacterial Coatings Using Hollow Nanoframes of Prussian Blue Analogues. *Adv. Mater.* **2025**, *37*, 2501174.
(61) Kim, D.-h.; Lee, D.; Monllor-Satoca, D.; Kim, K.; Lee, W.; Choi, W. Homogeneous Photocatalytic Fe^{3+}/Fe^{2+} Redox Cycle for Simultaneous Cr(Vi) Reduction and Organic Pollutant Oxidation: Roles of Hydroxyl Radical and Degradation Intermediates. *J. Hazard. Mater.* **2019**, *372*, 121−128.
(62) Morgan, B.; Lahav, O. The Effect of Ph on the Kinetics of Spontaneous Fe(II) Oxidation by O_2 in Aqueous Solution − Basic Principles and a Simple Heuristic Description. *Chemosphere* **2007**, *68*, 2080−2084.
(63) Orikasa, Y.; Maeda, T.; Koyama, Y.; Murayama, H.; Fukuda, K.; Tanida, H.; Arai, H.; Matsubara, E.; Uchimoto, Y.; Ogumi, Z. Transient Phase Change in Two Phase Reaction between Lifepo4 and Fepo4 under Battery Operation. *Chem. Mater.* **2013**, *25*, 1032−1039.
(64) Kim, J. H.; Lee, J. H.; Palem, R. R.; Suh, M. S.; Lee, H. H.; Kang, T. J. Iron (II/III) Perchlorate Electrolytes for Electrochemically Harvesting Low-Grade Thermal Energy. *Sci. Rep.* **2019**, *9*, 8706.
(65) Kim, J. H.; Lee, J. H.; Palem, R. R.; Suh, M.-S.; Lee, H. H.; Kang, T. J. Iron (Ii/Iii) Perchlorate Electrolytes for Electrochemically Harvesting Low-Grade Thermal Energy. *Sci. Rep.* **2019**, *9*, 8706.
(66) Winterbourn, C. C. Reconciling the Chemistry and Biology of Reactive Oxygen Species. *Nat. Chem. Biol.* **2008**, *4*, 278−286.
(67) Khan, Z. U. H.; Gul, N. S.; Sabahat, S.; Sun, J.; Tahir, K.; Shah, N. S.; Muhammad, N.; Rahim, A.; Imran, M.; Iqbal, J.; Khan, T. M.; Khasim, S.; Farooq, U.; Wu, J. Removal of Organic Pollutants through Hydroxyl Radical-Based Advanced Oxidation Processes. *Ecotoxicol. Environ. Saf.* **2023**, *267*, 115564.
(68) Abd El-Monaem, E. M.; Elshishini, H. M.; Bakr, S. S.; El-Aqapa, H. G.; Hosny, M.; Andaluri, G.; El-Subruiti, G. M.; Omer, A. M.; Eltaweil, A. S. A Comprehensive Review on Ldh-Based Catalysts to Activate Persulfates for the Degradation of Organic Pollutants. *npj Clean Water* **2023**, *6*, 34.
(69) Sasi, R.; Suchithra, T. V. Advanced Oxidation of Phenolic Pollutants in Wastewater. *Adv. Oxid. Processes Wastewater Treat.* **2022**, *4*, 193−201.

https://doi.org/10.1021/acsami.5c12970
ACS Appl. Mater. Interfaces 2025, 17, 56762−56772

Supporting Information

An Electrical Stimulation-Driven Strategy for Peroxide-like Enzyme Reactivation towards Sustainable Wastewater Sterilization

Jingyang Fang[a], *Guopeng Xu*[b], *Paul K. Chu*[c], *Jianzhong Du*[d,e,f]*, *Guomin Wang*[b]*

[a] Department of Polymeric Materials, School of Materials Science and Engineering, Tongji University, 4800 Caoan Road, Shanghai 201804, China.

[b] State Key Laboratory of Cardiovascular Diseases and Medical Innovation Center, Shanghai East Hospital, Department of Cardiovascular Surgery, Shanghai Tenth People's Hospital, School of Medicine, Tongji University, Shanghai, 200040, P. R. China.

[c] Department of Physics, Department of Materials Science and Engineering and Department of Biomedical Engineering, City University of Hong Kong, Tat Chee Avenue, Kowloon, Hong Kong, 999077 P. R. China

[d] Department of Gynaecology and Obstetrics, Shanghai Key Laboratory of Anesthesiology and Brain Functional Modulation, Clinical Research Center for Anesthesiology and Perioperative Medicine, Translational Research Institute of Brain and Brain-Like Intelligence, Shanghai Fourth People's Hospital, School of Medicine, Tongji University, Shanghai 200434, China.

[e] Key Laboratory of Advanced Civil Engineering Materials of Ministry of Education, School of Materials Science and Engineering, Tongji University, Shanghai 201804, China.

[f] School of Materials Science and Engineering, East China University of Science and Technology, Shanghai 200237, China.

*Corresponding authors

Email addresses: jzdu@tongji.edu.cn (J. Du), gwang@tongji.edu.cn (G. Wang).

Table S1. Antibacterial rates of different groups

Groups	Antibacterial Rate	
	E. coli	*S. aureus*
Control	0	0
H_2O_2	8.23±3.23%	5.04±3.59%
Fe-TNLs	13.76±1.35%	10.49±3.28%
Fe-TNLs + H_2O_2	99.9%	99.9%

Table S2. Composition of synthetic wastewater [a]

Compound	Concentration (mg L^{-1})
Yeast extract	22
Peptone	32
Urea	6
Dipotassium phosphate	28
Sodium chloride	7
Calcium chloride dihydrate	4
Magnesium sulphate heptahydrate	2

[a] Organization for Economic Co-operation and Development 2001[1]

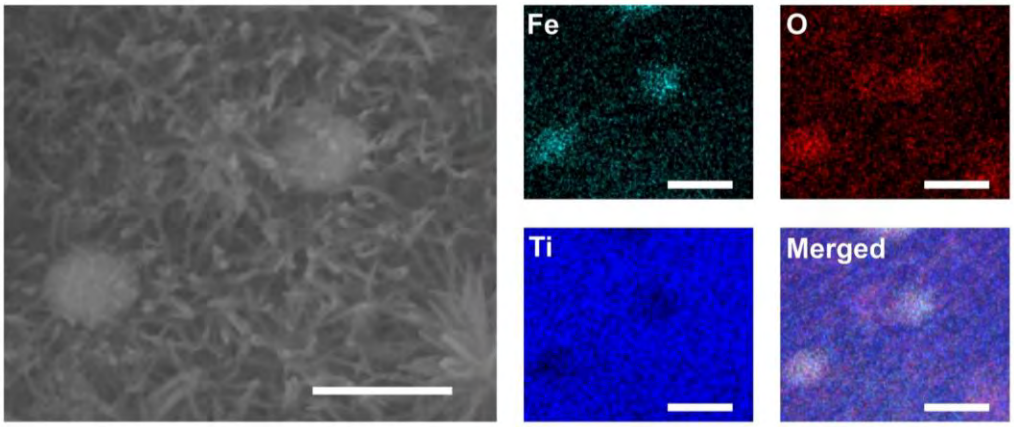

Figure S1 EDS mapping of the Fe-TNLs sample (scale bars: 500 nm).

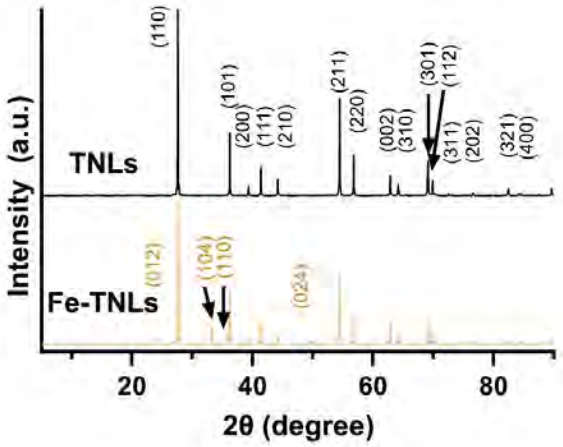

Figure S2 XRD patterns of the TNLs and Fe-TNLs samples.

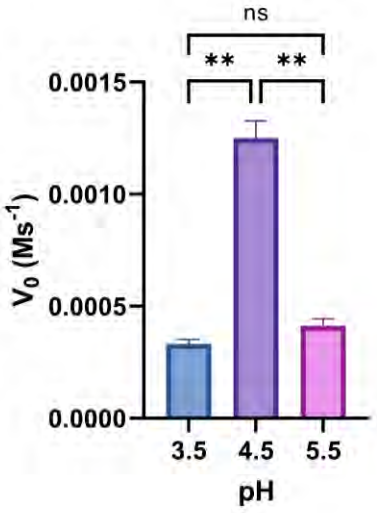

Figure S3 Influence of pH on the POD-like activity of Fe-TNLs. The optimal reaction pH was determined to be 4.5.

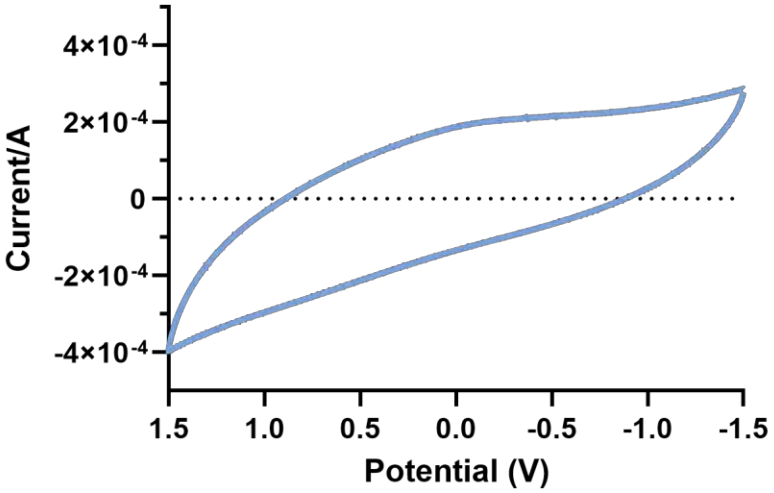

Figure S4 Cyclic voltammetry electrical stimulation of Fe-TNLs.

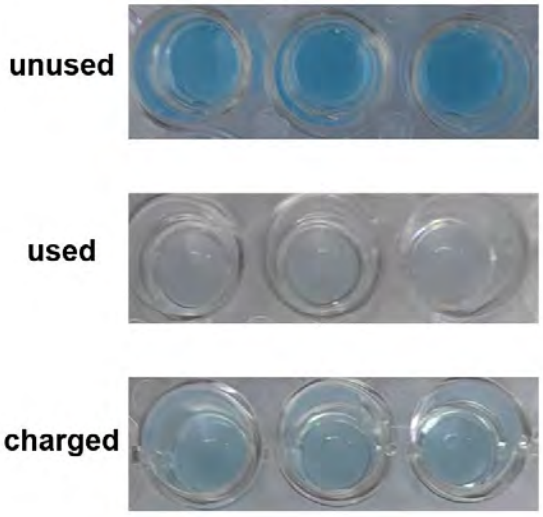

Figure S5 Initial POD activity measurement, followed by activity assessment after 15 minutes of exposure to H_2O_2, and finally reactivation measurement after charging, with a darker blue color indicating higher activity.

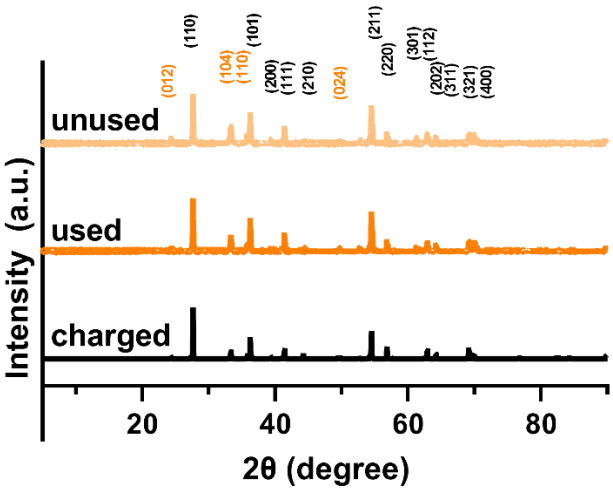

Figure S6 XRD patterns of unused group, used group and charged group.

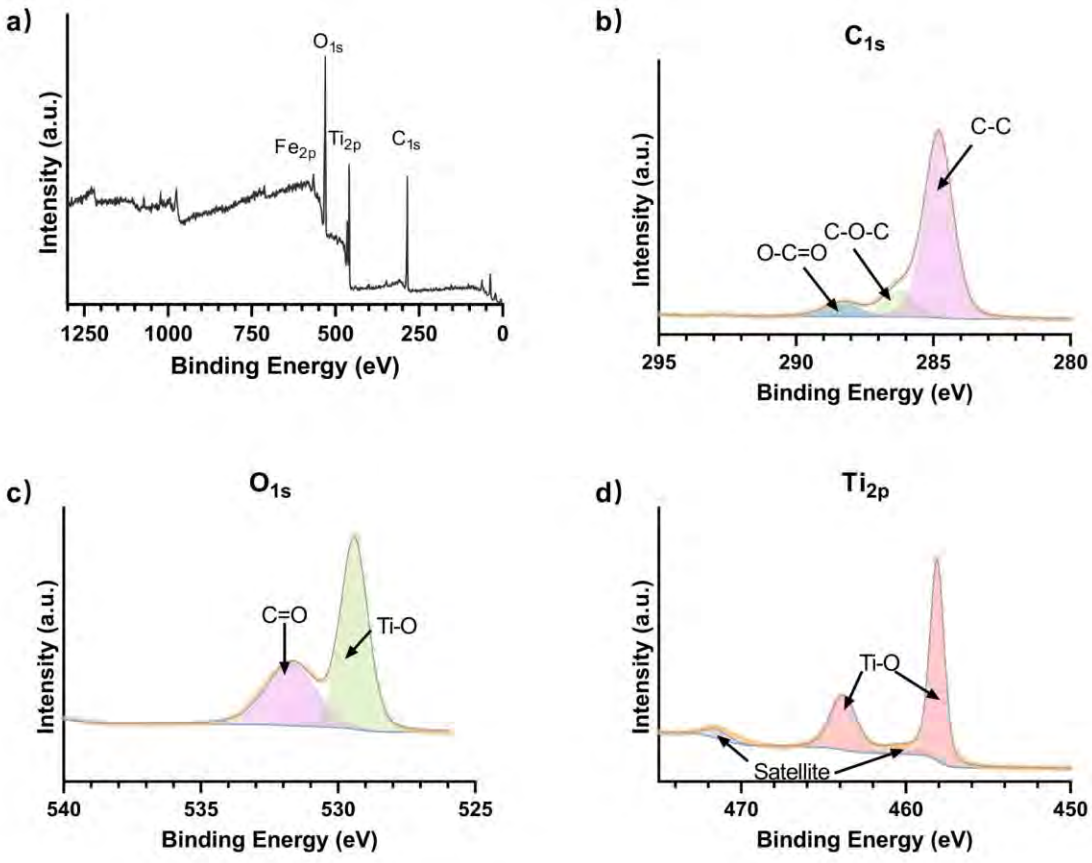

Figure S7 a) Full XPS spectrum of unused group's Fe-TNLs and fine spectra of three elements: b) C, c) O, and d) Ti.

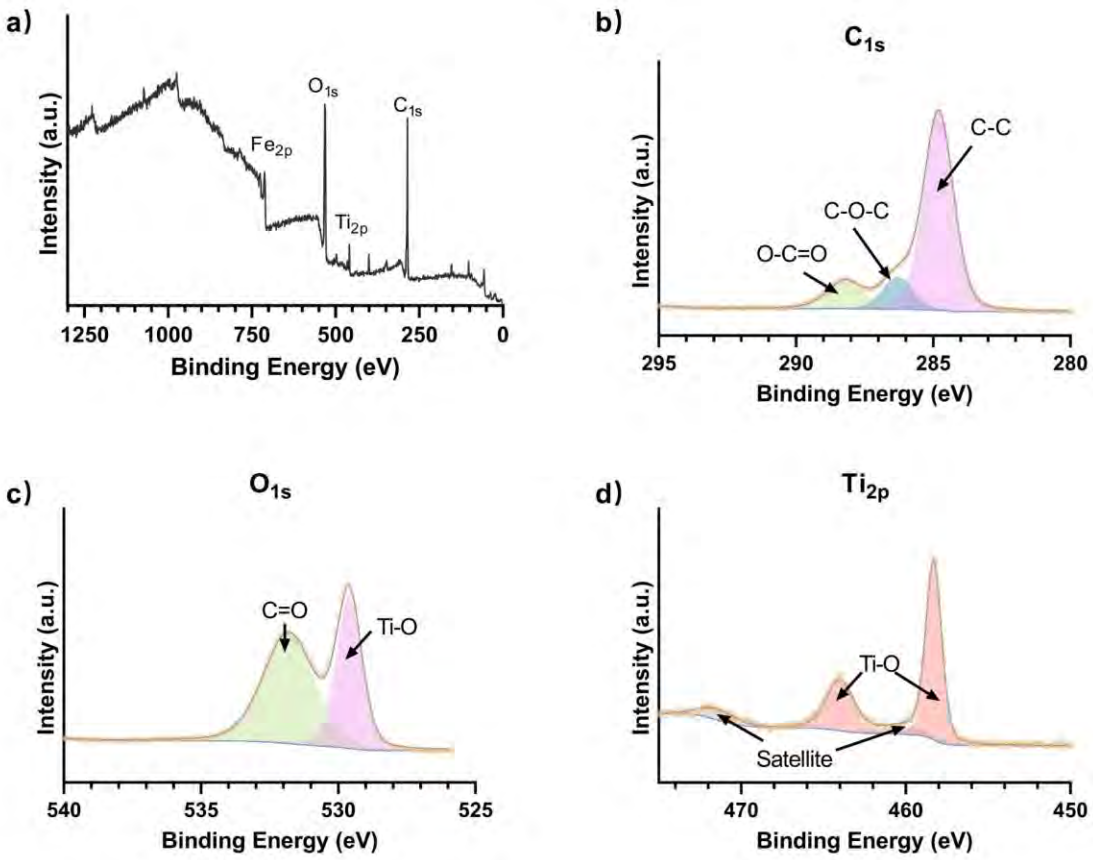

Figure S8 a) Full XPS spectrum of used group's Fe-TNLs and fine spectra of three elements: b) C, c) O, and d) Ti.

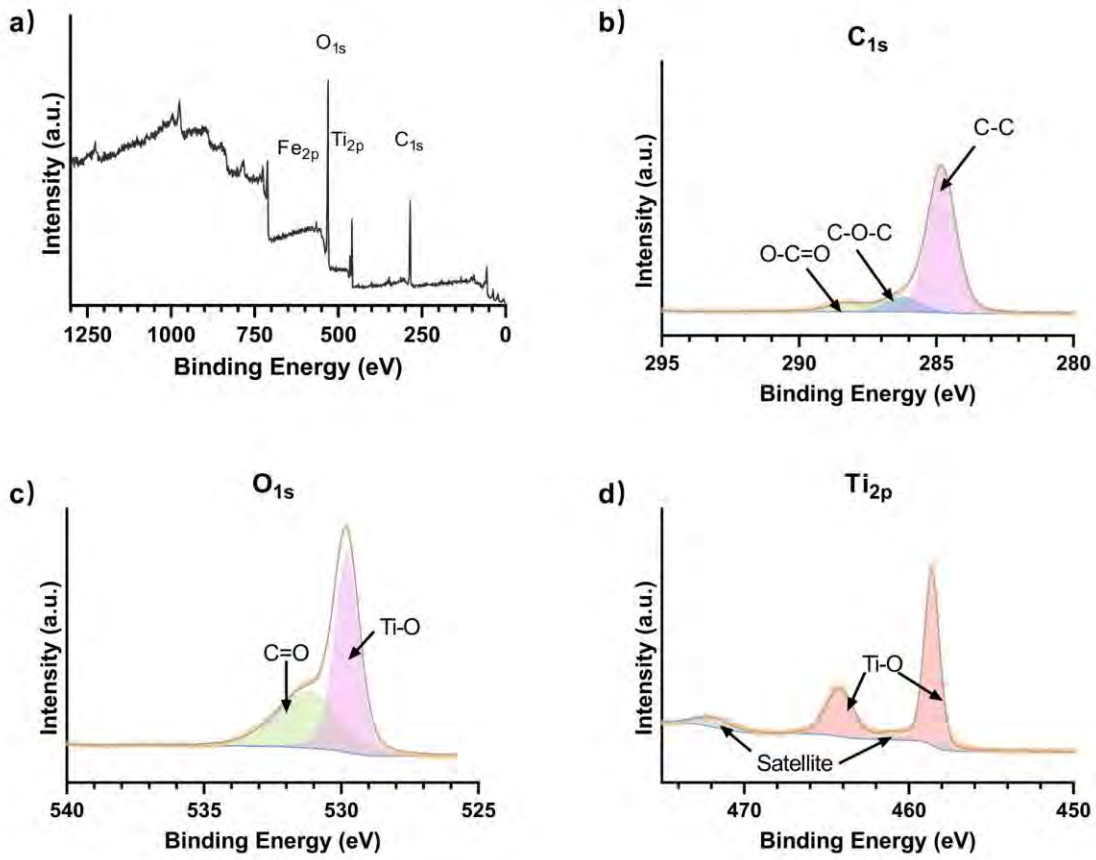

Figure S9 a) Full XPS spectrum of charged group's Fe-TNLs and fine spectra of three elements: b) C, c) O, and d) Ti.

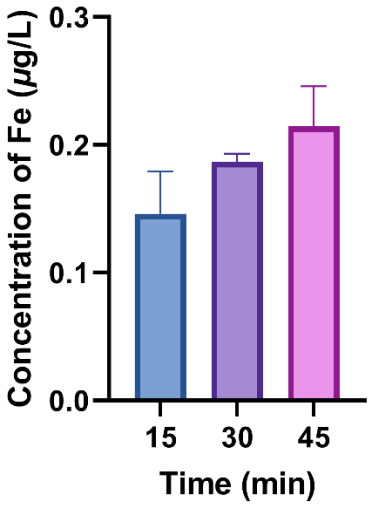

Figure S10 The concentration of Fe elements in the water gradually increases with time after immersing the Fe-TNLs in water.

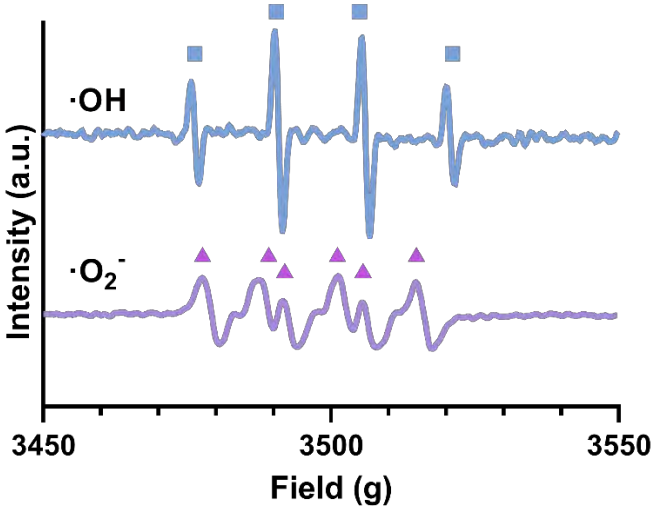

Figure S11 ESR spectra of ROS from Fe-TNLs+H_2O_2.

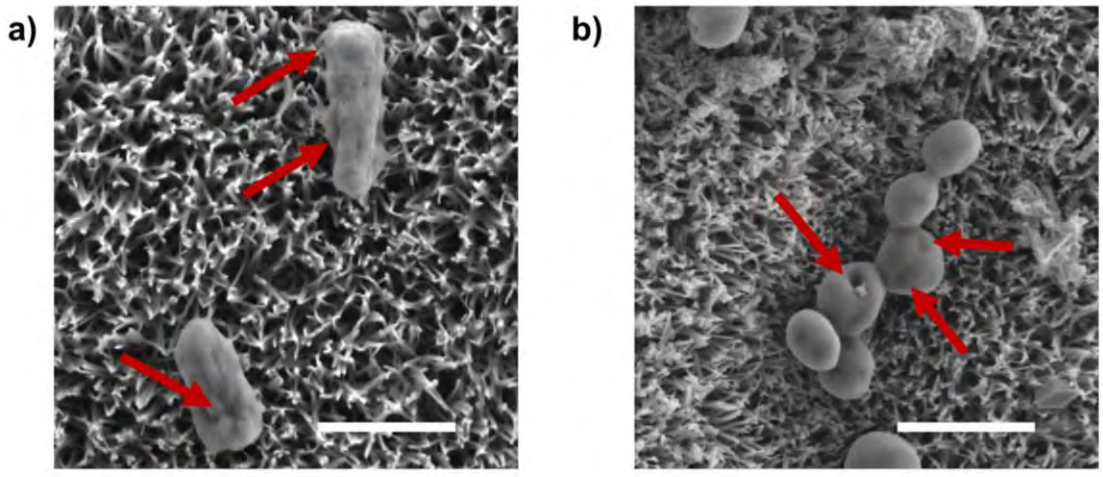

Figure S12 SEM images of a) *E. coli* and b) *S. aureus* interacting with Fe-TNLs under the addition of H_2O_2. Membrane damages are indicated by red arrows (scale bars: 1 μm).

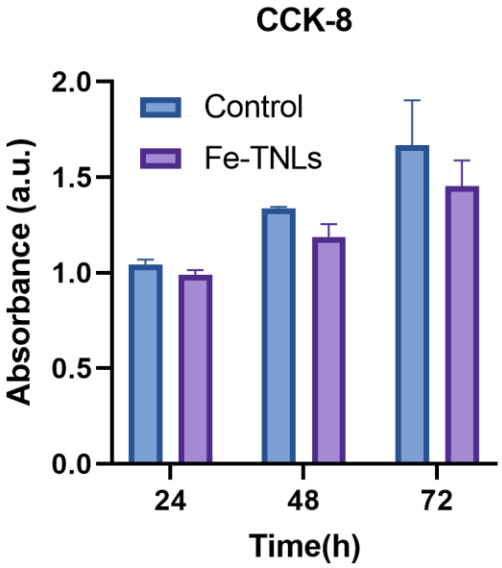

Figure S13 Growth of BMSCs measured by cck-8 under different culture times in Fe-TNLs leachate.

Figure S14 Colony counting in antimicrobial experiments on simulated wastewater.

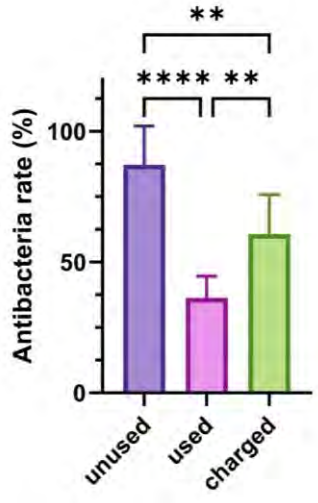

Figure S15 Antimicrobial efficiency of samples in simulated wastewater.

Reference

(1) *Test No. 303: Simulation Test - Aerobic Sewage Treatment -- A: Activated Sludge Units; B: Biofilms*; OECD Publishing: Paris, 2001.